Acta Materialia 96 (2015) 72–79

Contents lists available at ScienceDirect

Acta Materialia

journal homepage: www.elsevier.com/locate/actamat

On the role of melt flow into the surface structure and porosity development during selective laser melting

Chunlei Qiu *, Chinnapat Panwisawas, Mark Ward, Hector C. Basoalto, Jeffery W. Brooks, Moataz M. Attallah *

School of Metallurgy and Materials, University of Birmingham, Edgbaston, Birmingham B15 2TT, UK

ARTICLE INFO

Article history:
Received 3 April 2015
Revised 1 June 2015
Accepted 2 June 2015
Available online 12 June 2015

Keywords:
Selective laser melting
Titanium alloys
Porosity
Surface structure
Melt flow
Modelling

ABSTRACT

In this study, the development of surface structure and porosity of Ti–6Al–4V samples fabricated by selective laser melting under different laser scanning speeds and powder layer thicknesses has been studied and correlated with the melt flow behaviour through both experimental and modelling approaches. The as-fabricated samples were investigated using optical microscopy (OM) and scanning electron microscopy (SEM). The interaction between laser beam and powder particles was studied by both high speed imaging observation and computational fluid dynamics (CFD) calculation. It was found that at a high laser power and a fixed powder layer thickness (20 μm), the samples contain particularly low porosity when the laser scanning speeds are below 2700 mm/s. Further increase of scanning speed led to increase of porosity but not significantly. The porosity is even more sensitive to powder layer thickness with the use of thick powder layers (above 40 μm) leading to significant porosity. The increase of porosity with laser scanning speed and powder layer thickness is not inconsistent with the observed increase in surface roughness complicated by increasingly irregular-shaped laser scanned tracks and an increased number of discontinuity and cave-like pores on the top surfaces. The formation of pores and development of rough surfaces were found by both high speed imaging and modelling, to be strongly associated with unstable melt flow and splashing of molten material.

1. Introduction

Selective laser melting (SLM), due to its capacity to fabricate complex freeform geometries directly from computer-aided design (CAD) models, has been hailed as one of the most promising manufacturing technologies for net shape industrial scale production. So far, extensive studies have been performed aimed at defining the influence of the processing conditions on the microstructure and defect densities as well as mechanical properties. These studies have been carried out on a number of materials such as Ni-based superalloys [1,2], Ti-based alloys [3–5], Al-based alloys [6,7], steels [8] and composites [9,10]. It is clear from this work that there are also several concerns associated with this process that need to be addressed. These include residual stress development [11], cracking (particularly for certain materials such as nickel-based superalloys) [2], porosity [5,7] and mechanical anisotropy [5]. Among these concerns, porosity development is one of the most common issues that has been observed in almost all of the metallic materials processed by SLM and obviously is one of the major factors that could affect build quality and performance. However, so far, the reports on the mechanism of formation of porosity during SLM are rather limited with most of the explanations relying on assumptions. Thijs et al. [3] assumed that the formation of pores in a Ti-based alloy is due to powder denudation around the melt pool within a layer and an accumulation of the surface roughness across the layers but suggested that the formation of pores in an aluminium alloy could be due to the collapse of key holes [6]. Vilaro et al. [12] suspected that the development of pores could be the result of gas entrapment during melting and rapid solidification of the SLM process. Qiu et al. [5] directly observed open pores on the top surfaces of selectively laser melted samples and argued that the spherical pores could be due to incomplete re-melting of some localised sites on the previous layer and to the insufficient feeding of molten material to these sites. All these suggested mechanisms for the development of porosity, are based on unsubstantiated assumptions concerning the detailed mechanisms occurring during melting and solidification during SLM. Recently, Qiu et al. [13] observed the splashing of molten

* Corresponding authors.
E-mail addresses: c.qiu@bham.ac.uk (C. Qiu), m.m.attallah@bham.ac.uk (M.M. Attallah).

http://dx.doi.org/10.1016/j.actamat.2015.06.004
1359-6454/

material and the evolution of the melt pool during SLM of an aluminium alloy and suggested that the formation of pores in as-SLMed samples could be associated with melt pool instability and splashing. Panwisawas et al. [14] developed a melt flow dynamics model for SLM most recently and successfully used it to explain the morphological development of pores that were formed under different processing conditions. However, studies on the influence of melt flow behaviour on surface structure and porosity development, are generally lacking.

On the other hand, it is noted that the building rate of the current SLM process is generally low. At present, it typically processes only around a 20–30 μm thick powder layer [3–5]. The building rate could be improved by increasing powder layer thickness and laser scanning speed as the laser power is increased. However, while increasing the building rate, low levels of defects such as porosity also need to be guaranteed to ensure the required structural integrity and properties. It is therefore necessary to conduct a thorough investigation into the influence of powder layer thickness and laser scanning speed on porosity level. Previously, Ma et al. [8] studied the influence of powder layer thickness on relative density of stainless steel and indicated that increasing powder layer thickness to a certain level did not affect the relative density significantly.

In this paper, we perform a systematic parametric study to investigate the influence of laser scanning speed and powder layer thickness on porosity development and correlate the porosity development with the top sample surface structures (which could be considered as the traces of melt flow in SLM) and to the melt pool and flow behaviour studied by both high speed imaging and CFD simulation.

2. Experimental and modelling methods

The material used in this study was gas atomised Ti–6Al–4V powder supplied by TLS in the size range of 20–50 μm. A Concept Laser M2 Cusing SLM system which employs an Nd:YAG laser with a wavelength of 1075 nm and a maximum laser output power of 400 W measured in continuous wave mode was used to prepare samples for microstructural characterisation. Cubic samples with a dimension of 10 × 10 × 10 mm were fabricated at a fixed laser power of 400 W and a powder layer thickness of 20 μm but at different laser scanning speeds ranging from 2000 mm/s up to 4000 mm/s. Samples were also fabricated in argon at 400 W and at both 2400 mm/s but with different powder layer thicknesses ranging from 20 μm up to 100 μm to study the influence of powder layer thickness on porosity development. An island scanning strategy which has been detailed elsewhere [5] was used to fabricate the current samples.

Metallographic specimens were mechanically prepared using conventional methods and examined using an optical microscope (OM) and a JEOL 7000 FEG-SEM (scanning electron microscope) to reveal the size, distribution and morphology of pores. The porosity distribution was examined using tessellated micrographs to study large areas and the porosity area fraction (A_f) quantified using ImageJ. The top surfaces of the as-fabricated samples as a result of laser melting over the final layer of powder were also investigated using SEM. The roughness of the top surfaces was measured by surface profilometry in a Surfcorder SE 1700 machine.

High speed imaging was conducted using a Photron FASTCAM Mini UX100 high speed camera to develop understanding of the interaction between laser beam and powder materials as well as the influence of laser processing condition and layer thickness. The imaging was performed on SLM of 20 μm thick powder layers at a laser power of 400 W and under two laser scanning speeds including 2300 mm/s and 3500 mm/s, and also on powder with different layer thicknesses from 20 μm up to 100 μm at 400 W and 2400 mm/s. The images were taken at 10,000 frames/s.

To further investigate and gain better insight into the melt flow in association with surface structure development, a computational fluid dynamics (CFD) calculation, using the C++ open source CFD toolbox called Open Field Operation and Manipulation (OpenFOAM®) has been carried out to simulate the interaction between the laser heat source and the Ti–6Al–4V powder materials. All interfacial forces present in the process have been taken into account and simulated; these include surface tension (capillary force), Marangoni's flow (thermo-capillary force), recoil pressure, drag force due to solid/liquid transition via Darcy's term, and buoyancy force. The energy dissipation in the mushy zone during melting, and heat loss due to evaporation, conduction, convection and radiation have been simulated in this work. However due to the additional computational requirements, reflections of radiation have not been simulated in this work. In order to rationalise the thermal fluid flow, one needs to solve the coupling of the Navier–Stokes equation, energy conservation, continuity equation and volume-of-fluid equation. The volume-of-fluid methodology has been used to simulate the evolution of the liquid/gas interface. In this work, the summation of metallic α_1 and gaseous phases α_2 is always unity:

$$\alpha_1 + \alpha_2 = 1 \tag{1}$$

In addition, a weight function of any parameter x is used to smear out the effect of metallic and gaseous phases, defined as

$$\bar{x} = x_1\alpha_1 + x_2\alpha_2 \tag{2}$$

Assuming that the molten Ti–6Al–4V is incompressible so that the continuity condition is

$$\vec{\nabla}\cdot\vec{u} = 0 \tag{3}$$

Here $\vec{u}$ is flow velocity. To compute the evolution of the liquid/gas interface, the volume-of-fluid equation is used

$$\frac{\partial\alpha_1}{\partial t} + \vec{\nabla}\cdot(\alpha_1\vec{u}) = -\frac{\dot{m}_V}{\rho_2} \tag{4}$$

where t is time, and the sink term in the right hand side describes the loss of metallic phase due to evaporation when the evaporation temperature T_V is reached. ρ_2 is the density of metal vapour. The mass evaporation rate $\dot{m}_V$ is expressed as $\dot{m}_V = p_V\sqrt{\frac{m}{2\pi k_B T}}$ and the recoil pressure p_V is defined by $p_V(T) = p_0\exp\left\{\frac{\Delta H_V}{R}\left(\frac{1}{T_V}-\frac{1}{T}\right)\right\}$, where p_0, ΔH_V and R are atmospheric pressure, enthalpy change due to evaporation and universal gas constant, respectively [15–18]. In order to predict the evolution of melt pool at the beginning of interaction between the heat source and the materials during SLM, one needs to identify all forces presented during the process via the conservation of momentum or Navier–Stokes equation, which was written as

$$\frac{\partial\bar{\rho}\vec{u}}{\partial t} + \vec{\nabla}\cdot(\bar{\rho}\vec{u}\otimes\vec{u}) = -\vec{\nabla}p + \vec{\nabla}\cdot\bar{\bar{T}} + \bar{\rho}g\hat{e}_z\beta(T-T_{ref}) - K_C\left(\frac{(1-f_L)^2}{f_L^3+C_K}\right)\vec{u} + \left[\sigma\kappa\hat{n} + \frac{d\sigma}{dT}(\vec{\nabla}T - \hat{n}(\hat{n}\cdot\vec{\nabla}T)) + p_V\right]|\vec{\nabla}\alpha_1|\frac{2\bar{\rho}}{(\rho_1+\rho_2)} \tag{5}$$

Eq. (5) indicates that the rate of change of fluid momentum on the left hand side (LHS) is driven by all interfacial forces on the right hand side (RHS). Divergence of stresses is divided into pressure, p, and viscous deviatoric stress tensor, $\bar{\bar{T}}$:

$$\bar{\bar{T}} = 2\bar{\mu}\left[\left(\frac{1}{2}\vec{\nabla}\vec{u} + \frac{1}{2}(\vec{\nabla}\vec{u})^T\right) - \frac{1}{3}(\vec{\nabla}\cdot\vec{u})\mathbb{I}\right] \tag{6}$$

Here $\bar{\rho}$ is the density, $\bar{\mu}$ is mixture viscosity and $\mathbb{I}$ is the identity matrix. The third terms on RHS are used to describe buoyancy force caused by density differences due to thermal expansion, $\bar{\rho}g\hat{e}_z\beta(T-T_{ref})$, where g and $\hat{e}_z$ is the magnitude and unit normal of gravitational force, β is thermal expansion coefficient, T is temperature field and T_{ref} is the reference temperature. Darcy's term, $-K_C\left(\frac{(1-f_L)^2}{f_L^3+C_K}\right)\vec{u}$, which is energy dissipation or sink (damping) terms in the mushy zone is modelled in this work by making use of Carman–Kozeny equation [19], where K_C, f_L and C_K are permeability coefficient, fraction of liquid metal and constant, respectively. There are three surface force terms considered here: (i) surface tension term (capillary force) [20,21], $\sigma\kappa\hat{n}$, with surface tension σ, acting on surface curve κ at the unit normal $\hat{n}$, (ii) Marangoni force (thermos-capillary force) [22–24], $\frac{d\sigma}{dT}(\vec{\nabla}T-\hat{n}(\hat{n}\cdot\vec{\nabla}T))$, taking into account the effect of temperature gradient on the liquid/gas interface, and (iii) recoil pressure p_V when evaporation occurs. All surface forces have been applied only the interface indicated by the term $|\vec{\nabla}\alpha_1|$ and the sharper surface force term $\frac{2\bar{\rho}}{(\rho_1+\rho_2)}$ is used to smear out between hard and soft phases. For the conservation of total energy, one can express as

$$\frac{\partial\bar{\rho}\bar{C}_pT}{\partial t}+\vec{\nabla}\cdot(\bar{\rho}\vec{u}\bar{C}_pT)=-\frac{\partial\bar{\rho}\Delta H_f}{\partial t}-\vec{\nabla}\cdot(\bar{\rho}\vec{u}\Delta H_f)+\vec{\nabla}\cdot(\bar{k}\vec{\nabla}T)$$
$$-[(h_c(T-T_{ref})+\sigma_s\in(T^4-T_{ref}^4)+Q_V)|\vec{\nabla}\alpha_1|-Q_T]\frac{2\bar{\rho}}{(\rho_1+\rho_2)} \quad (7)$$

The thermal energy is balanced between heat input due to the heat source term Q_T [25] and heat loss due to conduction, $\vec{\nabla}\cdot(\bar{k}\vec{\nabla}T)$, convection, $h_c(T-T_{ref})$, radiation, $\sigma_s\epsilon(T^4-T_{ref}^4)$ and evaporation, $Q_V\sim\dot{m}_V\Delta H_V$ [15–18]. Here, $\bar{C}_p$ is specific heat for the mixture, $\bar{k}$ is thermal conductivity of the mixture, ΔH_f is the enthalpy change due to fusion, h_c is heat transfer coefficient, σ_s is Stefan–Boltzmann constant, and $\in$) is emissivity. By solving the set of Eqs. (3)–(5) and (7), the evolution of melt flow and liquid/gas interface can be rationalised. A detailed model description is to be published elsewhere [26] and model parameters were adopted from [27–29]. The model has been applied to a regular powder particle arrangement of 50 μm in diameter with an area of 250 μm × 250 μm, and a laser heat source of 400 W with a scanning speed of 3500 mm/s to simulate the processing condition. The modelling results are compared with the relevant experimentation.

3. Results

Fig. 1 shows the variation of porosity level as a function of laser scanning speed at a fixed laser power (400 W) and a fixed powder layer thickness (20 μm). It clearly shows that the as-fabricated samples generally have a low porosity level (<1.0%). The porosity is particularly low when the laser scanning speeds are below 2700 mm/s. Increasing scanning speed above this value (but below 4250 mm/s) did lead to increase of porosity but not significantly. The roughness of the top sample surfaces was also found to be larger at high scanning speeds than at lower scanning speeds (<2700 mm/s) (Fig. 2).

To understand the origin of the change of surface roughness with laser scanning speed, the top surface structures of the as-fabricated samples were investigated. Fig. 3 shows the top surface structures of the samples fabricated under 400 W–2300 mm/s and 400 W–3500 mm/s at a fixed powder layer thickness of 20 μm. Obviously, the surface structures produced under the two conditions are very different. At 2300 mm/s, the laser scanned tracks are evenly lined up and regularly overlapped with neighbouring

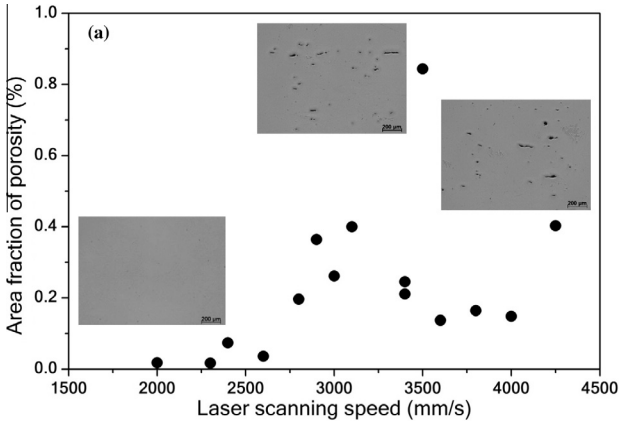

Fig. 1. Plot showing the variation of porosity with laser scanning speed at a fixed laser power of 400 W and a layer thickness of 20 μm [14]. The scatter of porosity levels is within ±0.05%.

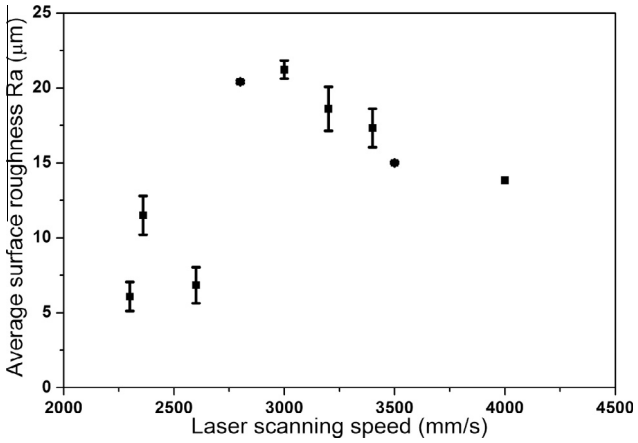

Fig. 2. Dependence of average surface roughness Ra on laser scanning speed. The samples were fabricated at 400 W and with a powder layer thickness of 20 μm.

tracks whereas at 3500 mm/s the tracks become increasingly irregular-shaped and even contain a few open pores with some obviously being due to discontinuity in the laser scanned track (Fig. 3(c)) and the rest (cave-like pores) due to the development of overhangs or bridges above a previous layer at some localised sites (Fig. 3(d)). Given that the laser scanned tracks are the traces of melt flow during SLM, the results suggest that the melt flow was extremely unstable at the high laser scanning speed. The presence of discontinuities on the sample surface could be due to either lack of material filling at some localised sites or material splashing out of some localised melt pools. The cave-like pores seem to be formed by the unstable melt flow moving away from laser scanning direction where the melt was solidified up in the air before bonding with the previous layer thus creating a hole underneath.

Fig. 4 shows the variation of porosity with powder layer thickness at 400 W–2400 mm/s. Both the area fraction and size of pores increase continuously with increased powder layer thickness. Particularly, when the powder layer thickness is above 60 μm, the porosity level rises rapidly and the pores become more elongated or irregular-shaped. Moreover, it is noted that the pores observed show no obvious un-melted or partially melted powder particles (which are usually spherical) within them (see Fig. 4(d)), suggesting that the majority of powder particles should have been melted during SLM even for the thicker powder layers.

In contrast to the effect of laser scanning speed on surface roughness (Fig. 2), the powder layer thickness is shown to have a

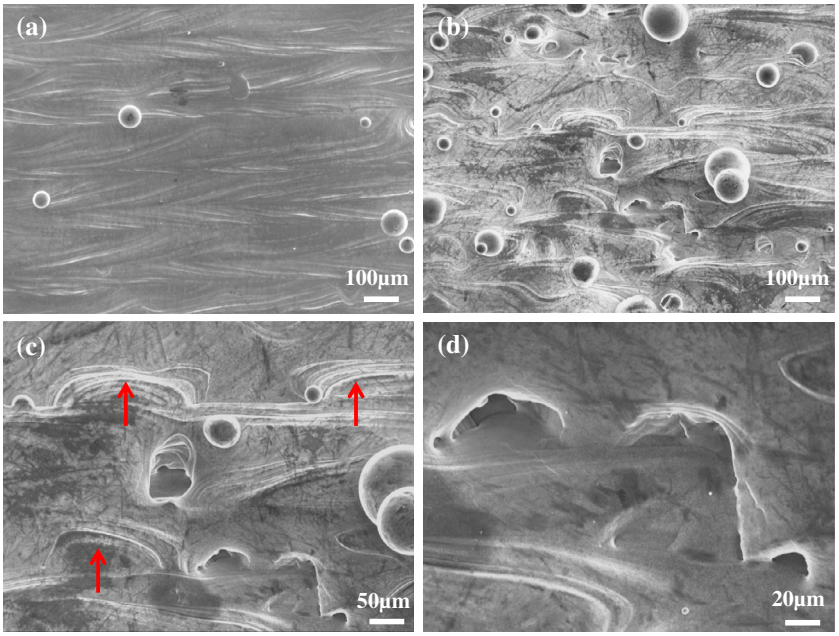

Fig. 3. SEM micrographs showing the top surface structure of the samples fabricated at (a) 400 W–2300 mm/s; (b–d) 400 W–3500 mm/s, with powder layer thickness of 20 μm. The arrows show the irregular-shaped melt flow traces.

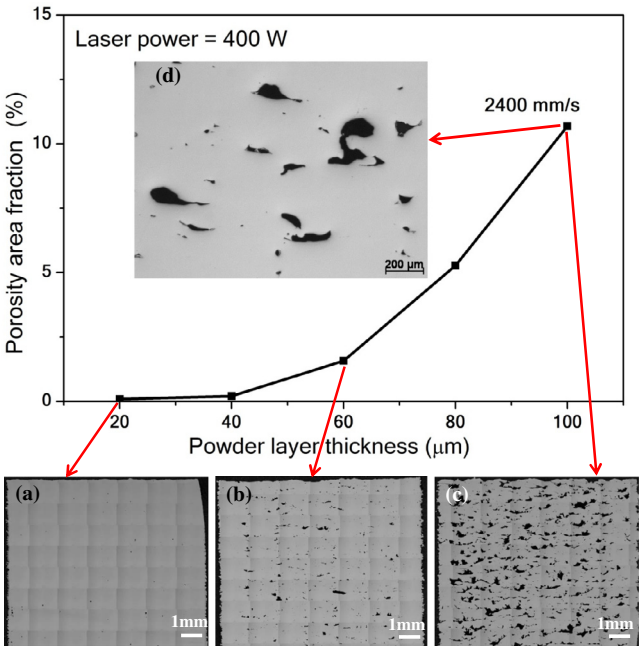

Fig. 4. Dependence of area fraction of porosity A_f on powder layer thickness, (a) A_f = 0.09%; (b) A_f = 1.58%; (c) A_f = 10.68%. The samples were fabricated at 400 W–2400 mm/s. The scatter of porosity levels is within ±0.05%.

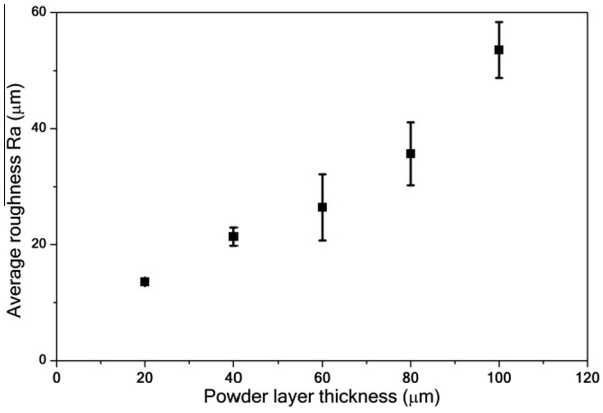

Fig. 5. Dependence of average surface roughness Ra on powder layer thickness. The samples were fabricated at 400 W–2400 mm/s.

stronger impact on surface roughness development (Fig. 5). Clearly, the top surface roughness has increased rapidly with increased powder layer thickness.

The surface structure of the samples fabricated with different powder layer thicknesses was also investigated and the result is shown in Fig. 6. The surface structure has changed significantly with powder layer thickness. At 20 μm, the laser scanned tracks are generally evenly laid out and homogeneously overlapped with neighbouring tracks whereas at 40 μm the tracks become increasingly misaligned and irregular-shaped, suggesting the melt flow became increasingly unstable. At 60 μm, the top surface starts to show open pores, with some obviously being due to discontinuity (Fig. 6(d)) and the rest (cave-like pores) due to the development of overhangs or bridges over a previous layer, similar to the observation at high laser scanning speeds (Fig. 3(b–d)). The irregularity of the surface structure becomes more pronounced when the layer thickness is above 60 μm (Fig. 6(e) and (f)) where the discontinuity on laser scanned tracks becomes more frequent and the numbers of cave-like pores rise sharply.

In addition, it is noted that the discontinuity and porosity development on the top surfaces are not inconsistent with the porosity development in bulk samples. Actually, even the top surface roughness was found to be in phase with the porosity development within bulk samples, as shown in Fig. 7. Particularly, when the average surface roughness (Ra) is above 30 μm, the porosity level within samples and the surface roughness increase.

To develop insights into the surface structure and porosity development during SLM, high speed digital imaging has been carried out in a simple linear laser scanning mode under several laser scanning speeds and with different layer thicknesses. Videos 1, 2

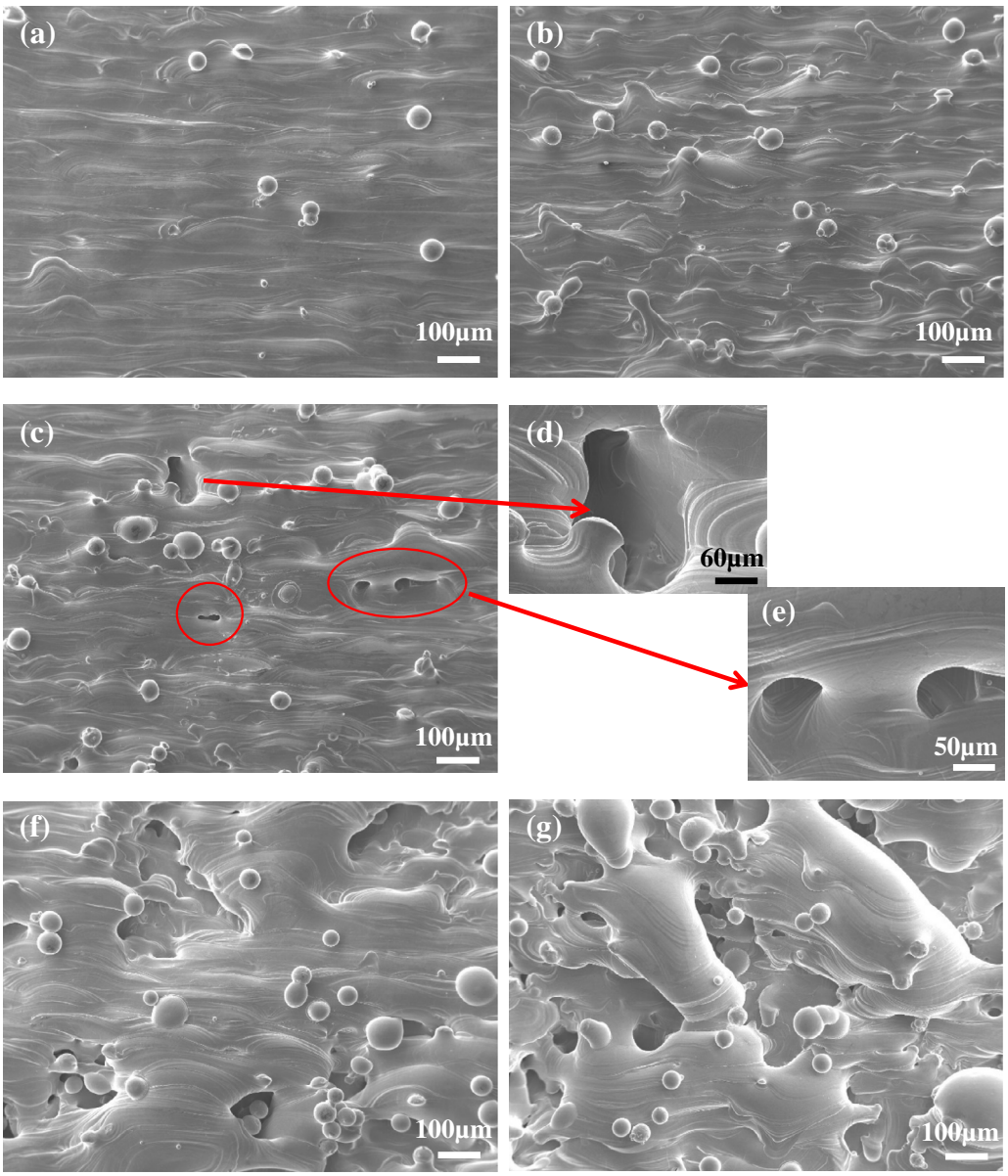

Fig. 6. SEM micrographs showing the variation of top surface structure of as-SLMed Ti64 samples with powder layer thickness, (a) 20 μm; (b) 40 μm; (c–e) 60 μm; (f) 80 μm; (g) 100 μm. The samples were fabricated at 400 W–2400 mm/s.

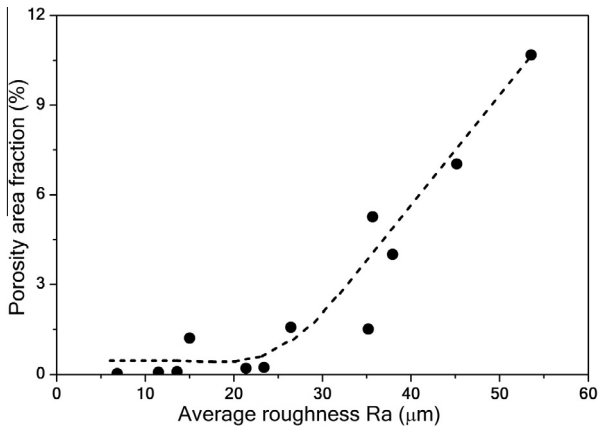

Fig. 7. Correlation between average surface roughness and porosity development of the as-SLMed samples. The scatter of the porosity levels are within ±0.05%.

and Fig. 8 show the interaction between the laser beam and a 20 μm thick powder layer at two different scanning speeds. No obvious difference in terms of melt pool size and morphology among these conditions could be observed. Splashing of molten particles could be seen in all the processing conditions and is more pronounced at increased laser scanning speeds. Moreover, the velocity of scattered melt particles was found to generally rise with increased laser scanning speed. These observations suggest that the melt pool may have become increasingly unstable with increased laser scanning speed. Videos 3–6 and Fig. 9 show the interaction between the laser beam and powder layers during SLM at 400 W–2400 mm/s with different powder layer thicknesses. The interaction between the laser beam and melt pool is particularly violent when thick powder layers (beyond 60 μm) were processed, characterised by significant melt splashing (Fig. 9(d) and (e) and Videos 5, 6). This suggests that the melt flow may have become unstable when thicker powder layers were processed by SLM, consistent with the implications derived from the observation on surface structures. Alongside the melt splashing,

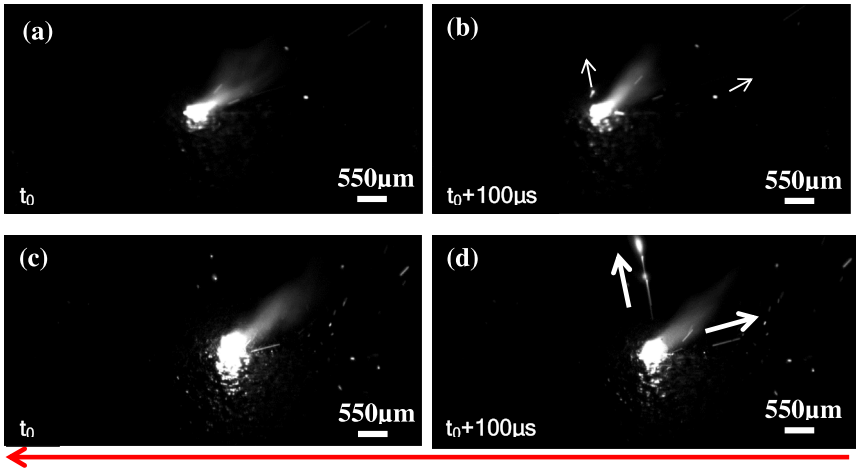

Fig. 8. High speed imaging showing the interaction between the laser beam and powder layers during SLM of 20 μm thick powder layers at 400 W and under different laser scan speeds (a)–(b) 2300 mm/s, and (c)–(d) 3500 mm/s. t_0 and t_0 +100 μs correspond to two neighbouring frames with an interval of 100 μs. White arrows indicate spattering directions and the estimated melt particle scattering velocities were about (b) 2200 mm/s, and (d) 15,000 mm/s, respectively. The red arrow shows the laser scan direction. (For interpretation of the references to colour in this figure legend, the reader is referred to the web version of this article.)

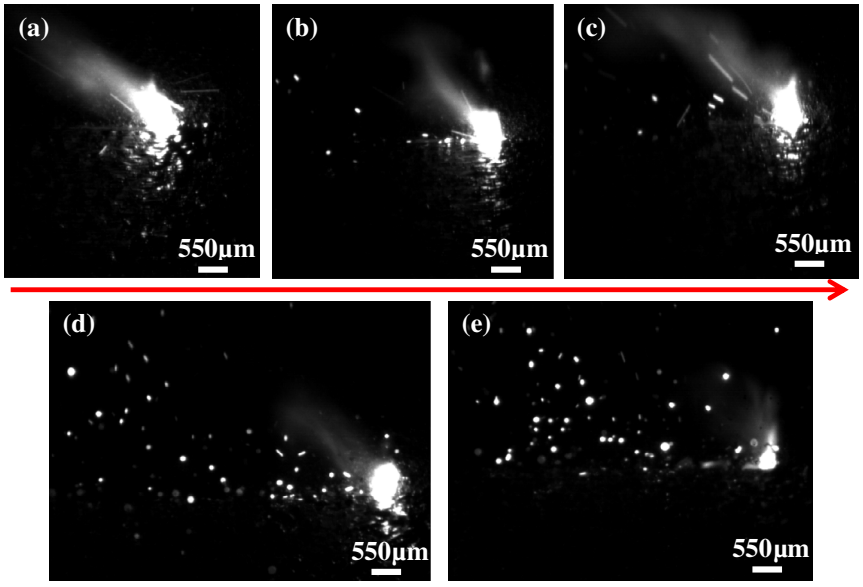

Fig. 9. High speed imaging showing the interaction between the laser beam and powder layers during SLM at 400 W–2400 mm/s with different powder layer thicknesses, (a) 20 μm; (b) 40 μm; (c) 60 μm; (d) 80 μm; (e) 100 μm. The arrow shows the laser scan direction.

there is always a blurred tail following the moving melt flow which is suspected to be due to material evaporation.

CFD modelling was also developed to simulate the interaction between the laser beam and the powder layer. The results are shown in Figs. 10 and 11. Splashing of molten material and evaporation of material are also predicted by modelling. With melt splashing, features of dents/discontinuities are also generated on the top surfaces due to the melt recirculation and splashing. Moreover, it is worth mentioning that the movement directions of the melt flows (highlighted by black arrows) in different parts of the melt pools do not follow the exact laser scanning direction but instead are highly dispersed further confirming that the melt flow is unstable during SLM. The predicted velocity of melt flows is generally higher at increased laser scanning speeds or larger powder layer thicknesses with some of the flow velocities going up to 15,000 mm/s (see the black arrows in the melt pool in Figs. 10(b) and 11(b)) which is at the similar level as that for some of the splashed particles observed in Fig. 8(c) and (d). At such a high flow velocity with flow direction deviant from the laser scanning direction, melt splashing could easily happen. The modelling results are generally in good agreement with the high speed imaging results and SEM observations on the top surfaces. Among the several forces taken into account in the modelling, Marangoni force and recoil pressure are believed to show the most significant influence on the stability of melt flow, which will be discussed in the following section.

4. Discussion

The current work demonstrates that the melt flow shows significant influence on the top surface structure and porosity development. The variation of surface structure and roughness with laser scanning speed and powder layer thickness is believed to be the direct result of melt flow behaviour. The modelling results suggest that the melt flows within melt pools could move in a dispersed

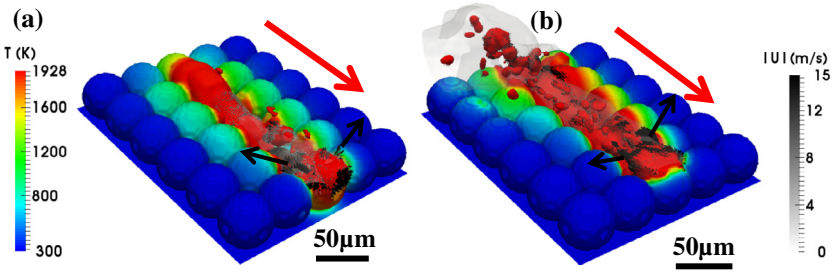

Fig. 10. Thermal fluid flow prediction of the interaction between laser heat source and regularly packed 50 μm powder particles using 400 W laser power with (a) 3500 mm/s and (b) 5000 mm/s scanning speeds. The red arrows show laser scanning direction while the black arrows show the moving directions of some of the melt flows within the melt pools. $|U|$ is the velocity of melt flow and T the absolute temperature of the materials during processing. (For interpretation of the references to colour in this figure legend, the reader is referred to the web version of this article.)

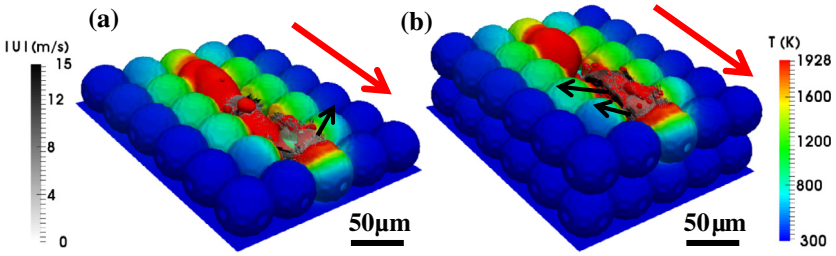

Fig. 11. Thermal fluid flow prediction of the interaction of laser heat source and regularly packed powder particles of (a) 50 μm and (b) 100 μm layer thicknesses using 400 W laser power with 2400 mm/s scanning speed. The red arrows show the laser scanning direction while the black arrows show the moving directions of some of the melt flows within the melt pools. $|U|$ is the velocity of the melt flow and T the absolute temperature of the materials during processing. (For interpretation of the references to colour in this figure legend, the reader is referred to the web version of this article.)

and random way (as illustrated in Figs. 10 and 11). This accounts for the development of irregular-shaped tracks on the top surfaces under certain conditions. Melt splashing together with material evaporation was observed by both high speed imaging and modelling. The driving force for the melt splashing is believed to be due to several combined effects including the Marangoni force developed at the surface and subsurface regions of the melt pool, recoil pressure due to material evaporation and gas expansion. The evaporation could lead to rapid cooling of the surface of melt pool and to the development of a thermal gradient between the surface/sub-surface region and the central region of the melt pool, which results in the development of the Marangoni force and the subsequent convection flow in the surface/sub-surface region of the melt pool. This could be complicated by the inhomogeneous cooling throughout the melt pool (the bottom area that is in contact with substrate or previously solidified layer experienced higher cooling rate). Also, the material evaporation would produce a recoil pressure back to the melt pool further destabilising the melt flow. Gas expansion due to immediate heating up by laser beam could further increase the instability of the melt pool and flow as well. However, since gas expansion is not included in the current modelling development due to the lack of data on tap density of a single spread layer of powder particles during SLM, the extent of its influence on melt flow behaviour requires further investigation.

The modelling results also suggest that the dispersive melt splashing could directly result in the formation of dents/discontinuity on the top surfaces of samples (Figs. 10 and 11) which is in good agreement with the experimental observation (Figs. 3(c) and 6(c–f)). These dents or open pores could be filled with melt materials in SLM of the next layer and then be closed or would remain as pores in the as-fabricated samples. There are also cave-like pores present on the top surfaces of the samples fabricated at higher laser scanning speeds (Fig. 3(d)) or with thicker powder layers (Fig. 6(c–g)). The formation of this kind of pore is believed to be due to the increasingly unstable melt flow which may have deviated from the laser scanning direction where the melt was solidified up in the air before bonding with the previous layer. This has been confirmed by the illustration of melt flow movement via modelling in Figs. 10 and 11. Also, the increased instability of melt flow with increased laser scanning speed and increased powder layer thickness has been supported by the observation of increasingly irregular-shaped laser scanned tracks and increased melt splashing and scattering velocity (Figs. 3, 6, 8 and 9). The cave-like pores could easily remain as pores in the bulk samples during the subsequent SLM building since they were covered with a layer of materials. To effectively eliminate them during subsequent building, it requires complete remelting of at least one or more of the previous layers.

The influence of laser scanning speed and powder layer thickness on surface structure and porosity development is also shown to be marked and is realised by their effect on the melt flow behaviour. Within the same timescale, the higher laser scan speed would produce longer melt pool and thus larger melt surface area and the evaporation and the thermal gradient in the melt pool would be stronger, which would increase the Marangoni force and the instability of the melt flow. This is also reinforced by the increased melt flow and splashing velocity according to both modelling (Fig. 10) and high speed imaging observation (Fig. 8). The powder layer thickness influences the melt behaviour mainly by affecting the amount of material melted by the laser beam. With thicker powder layers, more powder materials will be melted by the laser beam and there will be more melt surface area which would increase the evaporation and Marangoni force. With more powder particles and thus more gas in between, the gas expansion would be more obvious, which could further destabilise the melt flow. The increased instability of the melt flow with increased powder layer thickness is also supported by the increased velocity of melt flow within the melt pool (Fig. 11). Moreover, with more input energy being consumed in melting thicker powder particles,

there would be less heat to be used for re-melting of the previous layer [30,31]. If the freshly melted material cannot be well bonded to the previous layer, they would tend to be less constrained and more easily cause porosity development and melt splashing as observed in Fig. 9 and Videos 3–6. Given that high laser scan speed and thick powder layers lead to a highly irregular and unstable melt pool and thus to increased surface roughness and porosity, the selection of a proper laser scan speed and powder layer thickness is crucial for porosity control when the laser power is fixed. There will however be a limit in improving the build rate by simply increasing laser scan speed or powder layer thickness.

It is also noted that the surface roughness varied in the same sense as the extent of the porosity particularly when the surface roughness was beyond a certain value (Ra > 30 μm in the current study, according to Fig. 7). The increased surface roughness could cause inhomogeneous powder spreading and distribution and thus inconsistent melt flow and melt pool in the subsequent layers. The presence of discontinuity and cave-like pores on the top surfaces is very harmful for porosity development in bulk materials.

5. Conclusions

(i) Unstable melt flow is responsible for increased porosity and surface roughness.
(ii) The Marangoni force and recoil pressure are believed to be among the main driving forces for the instability of melt flow during SLM according to the present modelling.
(iii) With a high laser power and a low powder layer thickness, the selectively laser melted Ti–6Al–4V samples have a large processing window which enables the production of samples with low porosity (<1%) over a range of conditions, so that process control is not as critical.
(iv) Increased powder layer thickness leads to rapid increase in porosity level and surface roughness.

Acknowledgements

CQ and MA acknowledge the support by AMAZE project (Additive Manufacturing Aiming towards Zero Waste and Efficient Production of High-Tech Metal Products) which is funded by the 7th Framework Programme of the European Commission. Thanks are extended to Prof. Michael. H. Loretto for useful discussion and to Dr. Santiago. C. Gallo for assistance in surface roughness measurement. C.P., H.C.B., J.W.B. thank the support by the Centre for Advanced Simulation and Modelling collaborative project between Rolls-Royce plc, Manufacturing Technology Centre and the University of Birmingham and the support by the European Regional Development Fund.

Appendix A. Supplementary data

Supplementary data associated with this article can be found, in the online version, at http://dx.doi.org/10.1016/j.actamat.2015.06.004.

References

[1] L.E. Murr, E. Martinez, X.M. Pan, S.M. Gaytan, J.A. Castro, C.A. Terrazas, F. Medina, R.B. Wicker, D.H. Abbott, Microstructures of Rene 142 nickel-based superalloy fabricated by electron beam melting, Acta Mater. 61 (2013) 4289–4296.
[2] L.N. Carter, C. Martin, P.J. Withers, M.M. Attallah, The influence of the laser scan strategy on grain structure and cracking behaviour in SLM powder-bed fabricated nickel superalloy, J. Alloys Compd. 615 (2014) 338–347.
[3] L. Thijs, F. Verhaeghe, T. Craeghs, J. Van Humbeeck, Jean-Pierre Kruth, A study of the microstructural evolution during selective laser melting of Ti–6Al–4V, Acta Mater. 58 (2010) 3303–3312.
[4] W. Xu, M. Brandt, S. Sun, J. Elambasseril, Q. Liu, K. Latham, K. Xia, M. Qian, Additive manufacturing of strong and ductile Ti–6Al–4V by selective laser melting via in situ martensite decomposition, Acta Mater. 85 (2015) 74–84.
[5] C.L. Qiu, N.J.E. Adkins, M.M. Attallah, Microstructure and tensile properties of selectively laser-melted and of HIPed laser-melted Ti–6Al–4V, Mater. Sci. Eng. A 578 (2013) 230–239.
[6] L. Thijs, K. Kempen, Jean-Pierre Kruth, J. Van Humbeeck, Fine-structured aluminium products with controllable texture by selective laser melting of pre-alloyed AlSi10Mg powder, Acta Mater. 61 (2013) 1809–1819.
[7] N. Read, W. Wang, K. Essa, M.M. Attallah, Selective laser melting of AlSi10Mg alloy: process optimisation and mechanical properties development, Mater. Des. 65 (2015) 417–424.
[8] M.M. Ma, Z.M. Wang, M. Gao, X.Y. Zeng, Layer thickness dependence of performance in high-power selective laser melting of 1Cr18Ni9Ti stainless steel, J. Mater. Process. Technol. 215 (2015) 142–150.
[9] B. Vrancken, L. Thijs, J.-P. Kruth, J. Van Humbeeck, Microstructure and mechanical properties of a novel b titanium metallic composite by selective laser melting, Acta Mater. 68 (2014) 150–158.
[10] H. Attar, M. Bönisch, M. Calin, L.C. Zhang, S. Scudino, J. Eckert, Selective laser melting of in situ titanium–titanium boride composites: processing, microstructure and mechanical properties, Acta Mater. 76 (2014) 13–22.
[11] B. Vrancken, V. Cain, R. Knutsen, J. Van Humbeeck, Residual stress via the contour method in compact tension specimens produced via selective laser melting, Scr. Mater. 87 (2014) 29–32.
[12] T. Vilaro, C. Colin, J.D. Bartout, Metall. Mater. Trans. A 42 (2011) 3190–3199.
[13] C.L. Qiu, S. Yue, N.J.E. Adkins, M. Ward, H. Hassanin, P.D. Lee, P.J. Withers, M.M. Attallah, Influence of processing conditions on strut structure and compressive properties of cellular lattice structures fabricated by selective laser melting, Mater. Sci. Eng. A 628 (2015) 188–197.
[14] C. Panwisawas, C.L. Qiu, Y. Sovani, J.W. Brooks, M.M. Attallah, H.C. Basoalto, On the role of thermal fluid dynamics into the morphological development of porosity during selective laser melting, Scr. Mater. 105 (2015) 14–17.
[15] X. Jin, L. Li, Y. Zhang, A study on Fresnel absorption and reflections in the keyhole in deep penetration laser welding, J. Phys. D Appl. Phys. 35 (2002) 2304–2310.
[16] X. Jin, P. Berger, T. Graf, Multiple reflections and Fresnel absorption in an actual 3D keyhole during deep penetration laser welding, J. Phys. D Appl. Phys. 39 (2006) 4703–4712.
[17] M. Geiger, K.-H. Leitz, H. Kock, A. Otto, A 3D transient model of keyhole and melt pool dynamics in laser beam welding applied to the joining of zinc coated sheets, Prod. Eng. Res. Devel. 3 (2009) 127–136.
[18] M. Courtois, M. Carin, P.L. Masson, S. Gaied, M. Balabane, A new approach to compute multi-reflection of laser beam in a keyhole for heat transfer and fluid flow modelling in laser welding, J. Phys. D Appl. Phys. 46 (2013) 505305 (14pp).
[19] F. Rösler, D. Brüggemann, Shell-and-tube type latent heat thermal energy storage: numerical analysis and comparison with experiments, Heat Mass Transfer 47 (2011) 1027–1033.
[20] Y. Sun, C. Beckermann, Diffuse interface modelling of two-phase flows based on averaging mass and momentum equations, Physica D 198 (2004) 281–308.
[21] J.U. Brackbill, D.B. Kothe, C. Zemach, A continuum method for modelling surface tension, J. Comput. Phys. 100 (1992) 335–354.
[22] L.E. Scriven, C.V. Sternling, The Marangoni effects, Nature 187 (1960) 186–188.
[23] T. Ytrehus, S. Østomo, Kinetic theory approach to interphase processes, Int. J. Multiphase Flow 22 (1996) 133–155.
[24] H. Ki, P.S. Mohanty, J. Mazamder, Modelling of high-density laser-material interaction using fast level set method, J. Phys. D Appl. Phys. 34 (2001) 364–372.
[25] G.X. Xu, C.S. Wu, G.L. Qin, X.Y. Wang, S.Y. Lin, Adaptive volumetric heat source models for laser beam and laser + pulsed GMAW hybrid welding process, Int. J. Adv. Manuf. Technol. 57 (2011) 245–255.
[26] C. Panwisawas, I. Choquet, H. Nilsson, J.W. Brooks, H.C. Basoalto, Modelling of the formation of keyhole during laser fusion welding, in preparation.
[27] J.Z. Li, W.L. Johnson, W.K. Rhim, Thermal expansion of liquid Ti–6Al–4V measured by electrostatic levitation, Appl. Phys. Lett. 89 (2006) 111913 (2pp).
[28] R. Rai, J.W. Elmer, T.A. Palmer, T. DebRoy, Heat transfer and fluid flow during keyhole mode laser welding of tantalum, Ti–6Al–4V, 304L stainless steel and vanadium, J. Phys. D Appl. Phys. 40 (2007) 5753–5766.
[29] R. Rai, P. Burgardt, J.O. Mileewski, T.J. Lienert, T. DebRoy, Heat transfer and fluid flow during electron beam welding of 21Cr–6Ni–9Mn steel and Ti–6Al–4V alloy, J. Phys. D: Appl. Phys. 42 (2009) 025503 (12pp).
[30] C.L. Qiu, G.A. Ravi, C. Dance, A. Ranson, S. Dilworth, M.M. Attallah, Fabrication of large Ti–6Al–4V structures by direct laser deposition, J. Alloys Comput. 629 (2015) 351–361.
[31] P.A. Kobryn, S.L. Semiatin, Mechanical Properties of Laser-Deposited Ti–6Al–4V, Solid Freeform Fabrication Symposium Proceedings, Austin, 2001, 179–186.